CORA Cork Open Research Archive
Cartlann Taighde Oscailte Chorcaí

UCC Library and UCC researchers have made this item openly available. Please let us know how this has helped you. Thanks!

Title	Diffusion profile simulations and enhanced iron sensing in generator-collector mode at interdigitated nanowire electrode arrays
Author(s)	Wahl, Amélie J. C.; Seymour, Ian P.; Moore, Micheal; Lovera, Pierre; O'Riordan, Alan; Rohan, James F.
Publication date	2018-04-25
Original citation	Wahl, A. J. C., Seymour, I. P., Moore, M., Lovera, P., O'Riordan, A. and Rohan, J. F. (2018) 'Diffusion profile simulations and enhanced iron sensing in generator-collector mode at interdigitated nanowire electrode arrays', Electrochimica Acta. doi:10.1016/j.electacta.2018.04.181 untranslated
Type of publication	Article (peer-reviewed)
Link to publisher's version	http://dx.doi.org/10.1016/j.electacta.2018.04.181 Access to the full text of the published version may require a subscription.
Rights	**© 2018, Elsevier Ltd. All rights reserved. This manuscript version is made available under the CC-BY-NC-ND 4.0 license.** https://creativecommons.org/licenses/by-nc-nd/4.0/
Embargo information	Access to this article is restricted until 24 months after publication by request of the publisher.
Embargo lift date	2020-04-25
Item downloaded from	http://hdl.handle.net/10468/6101

Downloaded on 2021-11-27T05:38:08Z

UCC University College Cork, Ireland
Coláiste na hOllscoile Corcaigh

Accepted Manuscript

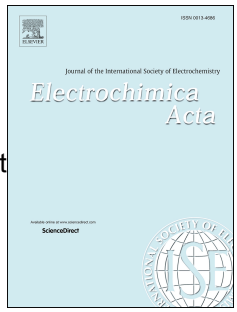

Diffusion profile simulations and enhanced iron sensing in generator-collector mode at interdigitated nanowire electrode arrays

Amélie J.C. Wahl, Ian P. Seymour, Micheal Moore, Pierre Lovera, Alan O'Riordan, James F. Rohan

PII: S0013-4686(18)30950-2

DOI: 10.1016/j.electacta.2018.04.181

Reference: EA 31748

To appear in: *Electrochimica Acta*

Received Date: 31 January 2018

Revised Date: 23 April 2018

Accepted Date: 24 April 2018

Please cite this article as: Amé.J.C. Wahl, I.P. Seymour, M. Moore, P. Lovera, A. O'Riordan, J.F. Rohan, Diffusion profile simulations and enhanced iron sensing in generator-collector mode at interdigitated nanowire electrode arrays, *Electrochimica Acta* (2018), doi: 10.1016/j.electacta.2018.04.181.

This is a PDF file of an unedited manuscript that has been accepted for publication. As a service to our customers we are providing this early version of the manuscript. The manuscript will undergo copyediting, typesetting, and review of the resulting proof before it is published in its final form. Please note that during the production process errors may be discovered which could affect the content, and all legal disclaimers that apply to the journal pertain.

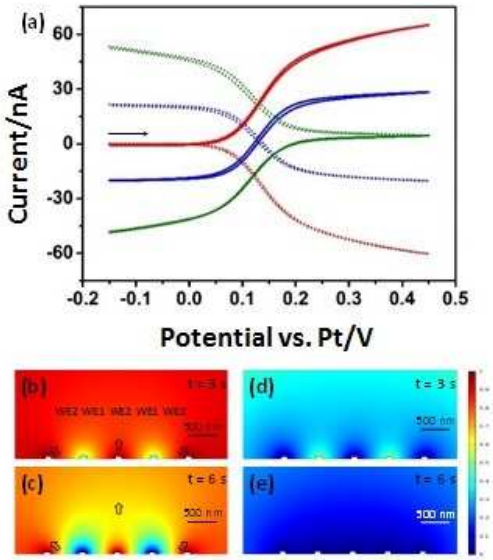

ACCEPTED MANUSCRIPT

ACCEPTED MANUSCRIPT

Diffusion profile simulations and enhanced Iron sensing in generator-collector mode at interdigitated nanowire electrode arrays.

Amélie J.C. Wahl, Ian P. Seymour, Micheal Moore, Pierre Lovera, Alan O'Riordan, James F. Rohan*

Tyndall National Institute, University College Cork, Lee Maltings, Cork, Ireland

*Corresponding author e-mail: james.rohan@tyndall.ie; Phone: +353 21 234 6224

Abstract: Gold interdigitated nanowire electrode arrays (INEAs) (~100 nm wide, ~50 nm high, ~45 µm long and ~500 nm spacing) on a Si/SiO_2 chip substrate were fabricated and characterised. Arrays were employed in both non-generator-collector (non-GC) mode (one array electrically connected) and in generator-collector (GC) mode (both arrays electrically connected). In non-GC mode, the individual arrays were confirmed to behave as microelectrodes arising from linear diffusion to the total area of the array. By contrast, in GC-mode, arrays displayed steady-state electrochemical behaviour arising from enhanced diffusion to the nanowires and redox cycling (RC) between adjacent electrodes. Finite element simulations were investigated to explore the effect of altering connected and non-connected electrodes on the diffusional behaviour of the arrays with 500 nm separations. They correlated well with the experimental observations for the influence of the collector electrode potential on redox reactions taking place at the generator for a range of scan rates. The suitability of the gold INEAs towards iron sensing in water is also reported. A calibration curve is obtained for 0.5 to 40 µM (28-2234 $\mu g.L^{-1}$) Fe^{2+} with a limit of detection (LOD) of

0.01 µM (0.6 µg.L^{-1}) well below the permitted level in drinking water. Finally, iron determination in tap water using a standard addition technique is presented.

Keywords:

Nanowire array, Interdigitated, on-chip, simulation, generator-collector, redox cycling, iron sensor.

1. Introduction

Recent advances in micro and nanofabrication techniques[1, 2] have enabled the fabrication of structures with controllable dimensions in the nanoscale. These have facilitated the development of novel devices such as electrochemical sensors for a wide range of applications including environmental, healthcare and security sensing[3-5]. For example, gold nanoelectrodes with critical dimensions less than 100 nm have been fabricated on silicon-based substrates with top-down approaches such as electron beam[6], nano[7] or focused ion beam lithography[8] and then combined with optical lithography to integrate on-chip interconnection tracks and on-chip counter and (pseudo)-reference electrodes[9, 10]. Nanoelectrodes by comparison with state-of-the-art microelectrodes display significantly improved electro-analytical characteristics arising from further enhanced mass transport, i.e., their critical dimensions are considerably smaller than the analyte diffusion layers formed during electroanalysis resulting in the fast establishment of steady-state analyte mass transfer by radial diffusion[11-13]. Furthermore, nanoelectrode arrays may be diffusionally independent under well-defined conditions such that the current is proportional to the number of nanoelectrodes present[14].

However, there are some limitations and we have shown that such arrays require micron-scale inter-electrode spacing for diffusional independence which limits the number of

nanowires per unit area[15, 16]. They may also experience relatively large charging currents (especially at high scan rates) and in such scanarios to identify changes in faradaic currents it is necessary to digitally subtract background currents from the overall recorded signals which then adds to the complexity of the system and analysis[17, 18]. To overcome these limitations, nanoelectrode arrays may be designed to enable RC analysis, i.e., repetitive analyte redox reactions occurring between adjacent electrodes. The basic concept of RC and its use for signal amplification has been well documented[19-25]. Typically, RC relies on two individually addressable working electrodes whereby one electrode, the generator, may be biased at one potential, while at the same time the other electrode, the collector, may be biased with a different potential such as used in the well known mm scale rotating ring-disc electrode arrangement. More recently a number of electrode configurations supporting RC have been reported based on micro and nanoelectrodes and gaps, including: combined rotating-microdisc electrodes[26], paired microband electrodes[27] recessed dual-ring nanopores[24] and interdigitated electrode arrays[28]. In the case of the latter arrays N generator electrodes are typically surrounded by N+1 collector electrodes with an inter-electrode distance on the order of micrometres to nanometres thus enabling efficient analyte diffusion and collection under GC control[20, 21, 29]

RC is optimised with enhanced signal amplification when the analyte redox reaction is fully reversible. Effectively, in GC mode, ~~a~~ reversible electroactive species cycles back and forth between the generator and collector, which provides a fresh (regenerated) supply of analyte to the electrodes. This RC gives rise to significant current amplification over electrode arrays operating in non-GC mode[27, 28, 30]. Furthermore, holding the generator or collector at constant potentials during data analysis minimises background charging currents. Thus, INEAs operating in GC mode are promising electrochemical sensing devices as they

demonstrate advantageous electrochemical properties when compared to microelectrodes[24] and they may be fabricated at higher density.

Iron concentration in drinking water varies worldwide depending on several factors, such as the iron salts used as coagulating agents in water-treatment plants or the pipe material used for water distribution. In Europe the permitted limit for iron in drinking water, based on the World Health Organisation guidelines is 200 $\mu g.L^{-1}$ (3.6 µM)[31]. Spectrometric techniques, e.g., inductively coupled plasma mass spectrometry, are widely used to monitor iron content in drinking water[32], however based on the experimental complexity of the analysis equipment it is generally restricted to lab environments. By contrast, electrochemical techniques, particularly with the development of INEAs, offer the possibility for rapid and portable methods of trace iron determination in aqueous environments.

Gold INEAs (~100 nm wide, ~50 nm high, ~45 µm long and with ~500 nm spacing) on a Si/SiO_2 chip substrate. The arrays comprise two individually addressable interdigitated comb-like structures designated as working electrode 1 (WE1, generator) and working electrode 2 (WE2, collector). Following fabrication, electrochemical characterisation was performed in ferrocene monocarboxylic acid (FCA) in 10 mM phosphate buffered saline at pH 7.4 (PBS) in non-GC (WE1 or WE2 connected) and in GC mode (WE1 was swept while a constant potential was applied to WE2). In non-GC mode, the closely spaced INEAs effectively behave as microelectrodes with diffusion to the whole array area rather than hemispherical diffusion to each nanowire[18, 33]. By contrast, in GC-mode, the INEAs displayed significantly enhanced electrochemical behaviour arising from RC between adjacent nanowires and localised diffusion to each individual nanowire. At INEAs the local environment at the generator electrode can also be altered significantly by the potential imposed at the collector electrode leading to very different electrochemical responses in identical solutions. Simulations of analyte diffusion to validate the electrochemical response

were in excellent agreement with experimental results, providing further insight into the molecular RC. To demonstrate the advantages of INEAs their suitability towards iron sensing for water quality analysis was also assessed.

2. Experimental

2.1 Chemical Reagents.

Ferrocene Carboxylic Acid ($C_{11}H_{10}FeO_2$, 97%) was purchased from Fluka. Iso-propyl Alcohol (Reagent Grade, 99%) and Hydrochloric Acid (HCl, 37%) were purchased from KMG Chemicals. Acetone (Analytical Grade, 99.5%), PBS (Tablets), iron (II) chloride tetrahydrate (Analytical Grade, 99% Fe) were purchased from Sigma-Aldrich and used as received.

2.2 Interdigitated Nanowire Device Fabrication.

On-chip devices containing gold interdigitated nanowire electrode arrays, a gold counter and a platinum pseudo-reference electrodes were fabricated using a combination of electron-beam and photolithography processes on Si/SiO_2 substrates as described in detail previously[15]. Interdigitated nanowires were patterned in resist by direct beam writing and metal evaporation (Ti/Au 5/50 nm) followed by standard lift-off techniques. Alignment marks were patterned along with this first metal layer to facilitate accurate positioning of subsequent optical lithography masks. Photolithography, metal evaporation (Ti/Au 10/90) and lift-off procedures were then employed to overlay electrical interconnection tracks including peripheral probe pads. Two macroscale gold electrodes were also deposited during this process, one of which was used as a counter electrode. A further metal deposition step (Ti/Pt 10/90 nm) onto one of these macroscale electrodes was undertaken to create an on-chip pseudo-reference electrode. A silicon nitride layer (~500 nm thick) was deposited to

passivate the entire chip and windows selectively opened to contact the gold INEAs, the gold counter and platinum pseudo-reference electrodes. Openings were also patterned above peripheral contact pads to permit electrical connection.

2.3 Structural and Electrical Characterisation.

Optical micrographs were acquired using a calibrated microscope (Axioskop II, Carl Zeiss Ltd.) with a charge-coupled detector camera (CCD; DEI-750, Optronics). SEM images were obtained using a calibrated field emission FEI Quanta FEG 650 at beam voltages between 5 and 30 kV. Two-point electrical measurements were performed using a probe station (Model 6200, Micromanipulator Probe Station) with a Keithley 2400 source meter and dedicated LabVIEW^{TM} programme.

2.4 Electrochemical cell and analysis.

To perform electrochemical analysis and to complete device packaging, chips were mounted in a custom-built electrochemical cell as described elsewhere[10]. Spring loaded probes (PM4J micro probe, CRIMP or PLUG SOCKET for PM4 series and a pre-wired RM4T-W700 terminal, Coda Systems Ltd.) made contact to the on-chip working, counter and pseudo-reference electrodes and (bi)potentiostat. The sample reservoir accommodated 150 µL solution with a chemical resistant O-ring seal (Polymax Ltd.), 4.5 mm in diameter. All electrochemical experiments were performed at room temperature (20°C) using a CHI760C bipotentiostat under PC control and Faraday Cage CHI200C (CH Instruments).

Prior to electrochemical experiments, electrodes were cleaned by sequential immersion for 10 minutes each in acetone and iso-propyl alcohol, followed by a thorough rinse with deionised water and dried with a filtered stream of nitrogen. Cyclic voltammetry (CV) measurements were recorded in 0 to 1 mM FCA in 10 mM PBS (pH 7.4) solutions. We did not observe a diminution of the electrode response in the FCA/PBS solutions over the lifetime of the

analysis performed for multiple characterisation experiments and cycles. Standard solutions were prepared using iron (II) chloride tetrahydrate and tap water acidified with HCl. Finally, the iron content in tap water was measured using a standard addition technique. Tap water aliquots were diluted 1:10 in deionised water, spiked with 0.1 to 0.5 µM iron and acidified to pH 3 with HCl. Solutions were prepared using deionised water (18.2 MΩ cm, ELGA Pure Lab Ultra).

2.5 Finite-Element Simulations.

FCA concentration profiles at INEAs used in non-GC and in GC modes were simulated using the commercial software package Comsol Multiphysics® 5.1. The objectives of these simulations were to explore the effect of altering connected and non-connected electrodes on the diffusional behaviour of the INEAs and examine the influence of the collector electrode potential on redox reactions taking place at the generator for a range of scan rates. The simulations were based on our approach reported previously[6, 13, 15]. The models were implemented to mirror experimental conditions in 1 mM FCA in 10 mM PBS as described above. The electron transfer process of FCA/FCA^+ is reversible, with both the oxidised and reduced forms soluble in solution with the associated diffusion coefficients assumed equal (5.4×10^{-6} $cm^2.s^{-1}$)[18], i.e., the sum of the concentration of both species is constant over the diffusion space and is assumed equal to the sum of their bulk concentration. An experimentally determined value of 0.15 V (vs. Pt) was employed for E^0, the formal potential of FCA/FCA^+. A simplified two-dimensional model known as the diffusion domain approach was adopted. In this approach, each nanowire was modelled as a 50 × 100 nm rectangle located at the centre of a much larger rectangle (space domain). The space domain area was selected to be large enough to ensure bulk-like conditions at the external boundaries remained unaffected by the electrochemical processes occurring at the electrodes. Simulations were resolved iteratively until a convergence error less than 2% was achieved.

3. Results and Discussion

3.1 Structural and Electrical Characterisation.

Structural characterisation of gold INEAs was performed using a combination of optical and scanning electron microscopy (SEM). Figure 1 (a) presents a schematic diagram showing the entire chip layout, while Figure 1 (b) is an optical image of the central area of the chip where the electrodes are located. Each chip contains twelve INEAs symmetrically located around a semi-circular gold counter electrode (CE) and a semi-circular platinum pseudo-reference electrode (PRE). Arrays comprise two individually addressable comb-like structures, WE1 and WE2 interdigitated nanowires, see Figures 1 (c) and (d). Each interdigitated nanowire device, either WE1 or WE2 or both could be biased selectively vs. the on-chip CE and PRE using the spring-loaded probes in the custom-made sample holder.

Figure 1: (a) Plan schematic diagram of a chip. (b) Optical micrograph highlighting the central area containing twelve gold interdigitated nanowire WE1-WE2 devices located around a gold CE and a platinum PRE. (c) SEM of gold interdigitated nanowire WE1-WE2 electrode arrays. (d) Higher magnification of (c).

SEM characterisation demonstrated that no residual passivation layer remained on the electrodes surface and excellent registration between the nanowire electrodes and the overlaid interconnection tracks. Nanowires have a proud rectangular cross-sectional shape (as opposed to being inlaid or recessed) and the passivation window defined their electrochemically active length (typically 45 µm). Their dimensions are ~100 nm in width and ~50 nm in height as previously reported[6, 10, 13] with an inter-nanowire distance of ~500 nm. Standard two-point *IV* measurements in air were undertaken as a quality control check to ensure electrical

isolation between WE1 and WE2 prior to electrochemical analysis (data not shown). All functioning devices yielded very high resistances (~10 GOhm) typical of an open circuit response.

3.2 Simulations and Electrochemical Analysis.

FCA was selected as a model molecule for a completely reversible single electron redox process[34]. The black line in Figure 2(a) shows the characteristic sigmoidal CV for a single gold nanowire electrode (~100 nm wide, ~50 nm high and ~45 µm long); the current reaches a highly reproducible time-independent steady-state on the order of 1.0 nA. The corresponding simulations show that the diffusion layer thickness is much larger than the nanowire electrode dimensions throughout the cycle, in particular when the potential reaches the mid (0.15 V) and end (0.45 V) potentials as presented in Figures 2(c) and (d), respectively.

Equivalent CVs were also obtained at gold interdigitated nanowire arrays in non-GC mode at WE1 (red line) and WE2 (blue line). Both CVs have the same shape with the current reaching a highly reproducible diffusion-limited oxidation peak with an average of about 9.5 nA. In fact, as expected they almost perfectly overlap, thereby demonstrating the nearly identical electrochemical behaviour of the two sides of the interdigitated arrays. However, while the electrode area of either side of the interdigitated nanowire arrays (~6 x 10^{-6} cm^2) is significantly (~70 times) larger than that of a single nanowire (~9 x 10^{-8} cm^2), the current only increased by a factor of ~9.5. At this sweep rate and for the 500 nm electrode separation the diffusion fields overlap and rather than having the hemispherical diffusion field at each nanowire they instead experience linear diffusion to the entire array and a peaked CV response. Corresponding simulated concentration profiles are shown in Figures 2(d)-(e) which confirm the diffusional overlap i.e., linear diffusion to the whole array[35, 36].

Consequently, in non-GC mode, WE1 and WE2 behave more as single microelectrodes occupying the same area as the overall array and thus may be considered as microelectrodes of width 80.5 µm (i.e., the distance separating the outer two nanowires in the array) and length 45 µm. There remains a contribution of each nanowire to the diffusion flux and therefore the current achieved given the actual area of the nanowire electrodes is higher than would be predicted by diffusion control to a microelectrode which would be expected to yield a limiting current less than 7 nA.

Figure 2: (a) Typical CVs for 1 mM FCA in 10 mM PBS between -0.15 and 0.45 V at 100 $mV.s^{-1}$. Signals were obtained at a single gold nanowire electrode (black line) and at gold nanowire interdigitated electrode arrays with 500 nm inter-nanowire spacing. Arrays were used in non-GC mode: the potential of WE1 was swept while WE2 was disconnected (red line) and vice-versa (blue line). (b) and (c) Cross-sectional views of 2D simulations of FCA concentration profiles at a single nanowire electrode respectively at t = 3 s (0.15 V) and 6 s (0.45 V) at 100 $mV.s^{-1}$. (d) and (e) are the equivalent cross-sectional representations at nanowire interdigitated electrode arrays with 500 nm inter-nanowire spacing in non-GC mode.

CVs were then recorded in GC mode. As presented in Figure 3 (a), when WE2 was held at -0.15 V (reducing potential for FCA^+), the current measured at WE1 (solid red line) and at WE2 (dashed red line) are essentially the inverse of each other. FCA redox currents at WE1 and WE2 reach a reproducible steady-state current ~7 times higher than the non-GC mode, thereby demonstrating improved individual nanowire behaviour. The currents are proportional to the number of nanowires in the arrays, i.e., every nanowire within WE1 and

WE2 behaves as a single electrode[20, 37]. As the nanowires are only 500 nm apart and WE2 maintains conditions favourable to the reduction of FCA^+ species, RC occurs between WE1 and WE2 as depicted in the schematic of Figure 3 (f), thus leading to the significant increase in current. The depletion of the Fe(II) species at the generator (WE1) electrode and the subsequent reduction of the Fe(III) product at the collector (WE2) electrode creates a local concentration gradient that shuttles the species between the GC electrodes unlike single electrodes or arrays employed in non-GC mode where the electrochemical response relies solely on mass transfer from the bulk solution.

3.3 Effect of Collector Potential.

In the GC mode CV experiments, species oxidised at WE1 were collected and reduced at WE2. Under these conditions, the WE2 collection efficiency, $\phi_{WE2(-0.15)}$, is defined as the ratio of the cathodic limiting current (absolute value) at WE2 to the anodic limiting current at WE1[21]. A 92.7% collection efficiency was measured, which demonstrates that redox species effectively diffused in cycles between the generator and collector, however a small percentage escaped to the bulk solution and was not collected at WE2. These observations were further investigated by the associated simulated concentration profiles. As shown in Figures 3 (b)-(c), while species produced at WE1 largely diffused to WE2 (and vice-versa) a minority also diffused into the bulk solution, vertically and at the outer nanowires. The diffusion layer established at WE1 necessitates an interaction with the bulk solution (see arrows). This behaviour is more apparent when the potential at WE1 reaches 0.45 V (t = 6 s) compared to that at 0.15 V (t = 3 s) as the diffusion layer increases with time.

By contrast, when the collector electrode WE2 was set to 0.45 V (oxidising potential), the resulting electrochemical behaviour (green lines; Figure 3 (a)) is the inverse of that described

previously. However, the current increase is not as efficient as that described above, i.e., the amplification vs. the non GC-mode is slightly lower (~ factor of 6.5). This is probably due to the imposition of 0.45 V at WE2 creating an environment where a low oxidation current (approximately 5.5 nA) is seen for bulk species oxidation at WE1 when the potential reaches 0.45 V. The WE2 collection efficiency, $\phi_{WE2(0.45\ V)}$, was found to be 92.5%, i.e., the opposite redox process is as effective. Consequently, the number of RC, N_{RC}, for each FCA molecule may be determined as follows:

$$N_{RC} = \frac{1}{1-[\phi_{WE2(-0.15)}\,\phi_{WE2(0.45)}]} \qquad (1)$$

Solving this equation yielded a value of ~7 for RC, which correlates extremely well with the observed current amplification when using GC mode compared to non-GC at 100 $mV.s^{-1}$ and indicates that the current amplification arises from a RC process between WE1 and WE2. Effectively, as the nanowires are close to each other and WE2 continuously oxidises the FCA species it creates an environment around the nanowires rich in FCA^+ while the bulk solution is FCA. This shows that for a simple open electrode arrangement as opposed to the more complex nano-well type electrodes, in a bulk solution of FCA, the environment of the electrode can be altered by controlling the collector electrode potential and the reacted product, in this case FCA^+, can be detected with an amplified signal as a result of RC. The simulated concentration profiles are again in excellent agreement with experimental observations: Figures 3 (d)-(e) show bulk/reductive species are readily oxidised at WE2 and a constant supply of oxidative species is maintained at WE1; when the potential at WE1 reaches 0.45 V (t = 6 s) a very small oxidation current is recorded at both electrodes but since both are at positive potentials there is no RC or hemispherical diffusion field and the current is more like the case on non-GC mode shown in Fig 2(a).

The collector electrode WE2 was also poised at the intermediate value of 0.15 V, see purple lines in Figure 3 (a). This biasing condition is between the completely oxidised and reduced extremities described previously. At t = 0 s, the applied potential at WE2 is sufficient to oxidise some FCA molecules which diffuse to and are reduced at WE1. Thus a RC process is again established but the measured current at both electrodes is lower due to the lower applied potential differential. As the applied potential increases at WE1, the measured current decreases. At t = 3 s, WE1 reaches 0.15 V and a similar situation to Figure 3 (a) (green lines) arises in that all oxidisable FCA molecules are depleted and negligible current is measured at WE1 or WE2. As the CV continues and the applied bias to WE1 increases beyond 0.15V, the RC process again begins but this is inverted compared to that at lower potentials. At t = 6 s, FCA molecules oxidised at WE1 diffuse to and are reduced at WE2. This situation arises since at 0.15 V WE2 may oxidise FCA or reduce FCA^+ with equal feasibility. This demonstrates that judicious selection of the collector electrode bias can selectively alter the chemistry of the local environment in close proximity to the electrodes. This can be utilised to selectively remove interferent species while the RC process enhances the analyte signal.

Figure 3: (a) Typical CVs for 1 mM FCA in 10 mM PBS from -0.15 to 0.45 V at 100 $mV.s^{-1}$. CV signals were obtained at gold INEAs with 500 nm inter-nanowire spacing. Arrays were used in GC mode: the potential of WE1 was swept while the potential of WE2 was held at -0.15 V (red lines), 0.15 V (blue lines) or 0.45 V (green lines). The current was measured at both WE1 (solid lines) and WE2 (dashed lines). Corresponding cross-sectional view of 2D simulations of FCA concentration profiles during the CV in GC mode at 100 $mV.s^{-1}$ at t = 3 s and 6 s, respectively, with the collector potential (b, c) -0.15 V and (d, e) 0.45 V. (f) Schematic diagram of RC at interdigitated nanowire array in GC mode.

3.4 Effect of Scan Rate.

CVs in 1 mM FCA in 10 mM PBS in GC-mode with WE2 biased at -0.15 V were repeated for a range of scan rates. As presented in Figure 4 (a), interdigitated gold nanowire electrodes typically display sigmoidal CVs (only results for 5 and 5000 $mV.s^{-1}$ are shown for clarity) with the current reaching a highly reproducible time-independent steady-state at both WE1 (solid lines) and WE2 (dashed lines) arising from the RC process. Of note, the slight hysteresis in the WE1 currents is associated with charging currents which are more pronounced at higher scan rates. This clearly indicates that the rate of FCA replenishment was sufficient at WE1 regardless of the analysis time (on the order of 100 ms at 5000 $mV.s^{-1}$ and 100 s at 5 $mV.s^{-1}$), while bulk-like conditions remained unchanged at WE2. In other words, at high scan rates both the generator and collector currents may reach steady-state within a hundred milliseconds, thus opening the door for the investigation of electron-transfer processes over extremely short electrolysis times. Furthermore, the corresponding simulated concentration profiles are in excellent agreement with experimental observations as no significant differences are observed between that at 5, 100 and 5000 $mV.s^{-1}$, Figures 3 (c) and 4 (b)-(c).

As briefly discussed above, high signal-to-noise ratios were achieved, unlike conventional electrodes for which faradaic signals may become swamped by background currents especially at high scan rates. Background currents principally arise from an electrical double layer of charged species which form at the electrode surface when a potential bias is applied. CV experiments were undertaken in 10 mM PBS solution without the redox active FCA to assess charging currents contributions. At WE1 (generator), the non-faradaic currents increased linearly with increasing scan rates from less than 0.1 nA at 5 $mV.s^{-1}$ to about 5.6 nA at 5000 $mV.s^{-1}$ (average of forward and reverse scans) indicating a capacitance on the order of 1 nF, while at WE2 (collector) the background currents are significantly lower

indicating a capacitance <0.3 nF; see Figure 5. The charging currents detected at the collector electrode has been attributed to imperfect insulation between the generator and collector electrodes which can lead to charge leakage[17, 29].

Figure 4: (a) Typical CVs at gold nanowire interdigitated electrode arrays with 500 nm inter-nanowire spacing in 1 mM FCA in 10 mM PBS between -0.15 and 0.45 V (vs. Pt) at 5 and 5000 $mV.s^{-1}$. Arrays were used in GC mode: the potential of WE1 was swept while the potential of WE2 was held at -0.15 V. The current was measured at both WE1 (solid lines) and WE2 (dashed lines). (b)-(c) Cross-sectional view of 2D simulations of FCA concentration profiles corresponding to CVs when the potential at WE1 reaches 0.45 V and was swept at 5 and 5000 $mV.s^{-1}$, respectively.

Figure 5: (a) (b) Average of forward and reverse non-faradaic currents at WE1 (red squares) and WE2 (blue squares) vs. scan rate (for WE1) from typical CVs in 10 mM PBS only (without redox active FCA) at a gold nanowire interdigitated electrode array with 500 nm inter-nanowire spacing. The array was used in

GC mode: the potential of WE1 was swept from -0.15 to 0.45 V for the scan rates shown while the potential of WE2 was held at -0.15 V.

Digital subtraction of the background currents from the overall recorded signals (not shown) further demonstrates that CVs at WE1 and WE2 consisted essentially of faradaic currents, i.e., only signals at WE1 were slightly affected by charging currents for high scan rates (≥ 2000 $mV.s^{-1}$). The slight distortions of the fast sweep CVs caused collection efficiencies to drop from ≥ 90% (< 2000 $mV.s^{-1}$) to about 80% (≥ 2000 $mV.s^{-1}$).

3.5 Effect of Analyte Concentration.

CVs in GC-mode over a range of scan rates and with WE2 biased at -0.15 V were undertaken in triplicate in 0.1, 0.2, 0.5, 0.75 and 1 mM FCA in 10 mM PBS solutions in order to further study the sensitivity of gold interdigitated nanowire electrodes. All recorded signals were sigmoidal as shown in figure 6 (a) and exhibited highly reproducible current magnitudes as summarised in Figure 6 (b) which includes the error bars for the triplicate readings and demonstrates that the steady state currents were proportional to FCA concentration from 0.1 to 1 mM (R^2 = 0.978) at both WE1 (red squares) and WE2 (blue squares) at 100 $mV.s^{-1}$. Furthermore, this behaviour was observed for all scan rates with only small variations observed in the slopes and intercepts which are likely due to interferences caused by the charging currents discussed above. This shows that high signal-to-noise ratios were achieved even at high scan rates, thus permitting rapid (within milliseconds) quantitative analysis to be undertaken and that both the generator and collector currents can be used for calibration purposes.

Figure 6: (a) Typical CVs (vs. Pt) in 0 to 1 mM FCA in 10 mM PBS at a gold INEA with 500 nm inter-nanowire spacing. The array was used in GC mode: the potential of WE1 was swept from -0.15 to 0.45 to -0.15 V at 100 $mV.s^{-1}$ while the potential of WE2 was held at -0.15 V. (b) Quasi steady-state currents measured at WE1 (red squares) and WE2 (blue squares) vs. FCA concentration.

3.6 Iron Detection.

To explore the suitability of fully integrated gold INEAs towards future sensing applications, CV measurements in GC mode were undertaken for a range of iron concentrations in HCl solutions across an applied potential range of 0.2 to 1.0 V (vs. Pt) at 100 $mV.s^{-1}$. The potential at WE2 was held at a reductive potential (0.4 V vs. Pt), i.e., a potential established experimentally to be favourable to the RC of Fe^{3+}/Fe^{2+} between WE1 and WE2. Iron was selected as the analyte of choice due to its reversible electrochemical properties and its importance in environmental and health applications[38-40]. It is commonly found in both its ferrous and ferric states, which are soluble in acidic aqueous solutions but precipitate at neutral pH and above[40]. As HCl has been found to facilitate the reversible redox processes of Fe^{3+}/Fe^{2+}, it was selected as the background electrolyte [41]. To this end, 1 mM (pH 3), 10 mM (pH 2) and 100 mM (pH 1) HCl solutions were investigated. 1 mM HCl was found to give rise to the maximum iron oxidation peak and thus was chosen as the background electrolyte. No damage to the nanowire electrodes arising from the presence of the acidic aqueous media was observed, however cycling from over -0.9 to 0.8 V (i.e., outside hydrogen evolution and prior to gold dissolution[41]) in 1 mM HCl prior to each measurement in iron solution was required as a surface activation step to obtain stable reproducible signals.

CV studies in GC mode were performed at the optimised conditions in 0 to 40 µM Fe^{2+} (0 to 2234 $\mu g.L^{-1}$) in 1 mM HCl solutions. As seen in Figure 7 (a), on the forward scan at WE1 a well-defined oxidation peak at around 0.6-0.7 V was typically recorded in the absence of iron. This peak arises from gold oxide layers formation at the gold surface[41], for which a corresponding reduction peak was recorded on the reverse scan at about 0.2-0.3 V. No additional peaks were recorded in the presence of iron other than the increase in the anodic pre-peak at ~0.7 V for increasing iron concentrations. Low coverage gold oxides (which are reformed during the activation step in 1 mM HCl) are known to effectively promote electron transfer[42] and thus the analytical signal of iron is actually the difference between the

recorded analyte signal and the background oxide formation current. This was demonstrated across a range of iron concentrations, see Figure 7 (b). The oxidation peak currents at WE1 were found to be directly proportional to the iron concentration (R^2 = 0.995) with the intercept equal to the oxide formation current in 1 mM HCl and collection efficiencies on the order of 60%.

Figure 7: (a) Typical CVs (vs. Pt) in 0-40 µM Fe^{2+} in 1 mM HCl (pH 3) between 0.2 and 1.0 V at 100 $mV.s^{-1}$ for gold nanowire interdigitated electrode arrays with 500 nm inter-nanowire spacing. Arrays were used in GC mode: the potential of WE1 was swept while the potential of WE2 was held at 0.4 V (vs. Pt). The current was measured at both WE1 (solid lines) and WE2 (dashed lines). (b) Peak currents measured at WE1 vs. Fe^{2+} concentration.

The peak behaviour is likely due to the compact gold oxide formation as the sweep is continued to higher positive potentials which ultimately inhibits the continuing reaction for the iron species. The collector electrode was maintained at a constant potential and as such the data at the collector electrode is not from a potential sweep experiment. The plotted current is due to the diffusion controlled current response to the reaction at the generator electrode and therefore as its current rises the observed current response at the collector electrode rises and when it peaks and falls at the generator the inverse peaked response is seen at the collector.

The gold reduction peak at WE1 was found to be very reproducible for all solutions, which strongly supports that the oxidation of iron (II) occurs around the same potential as the gold oxides formation. The presence of an increasing current at the collector electrode for the reduction of the reacted Fe^{3+} demonstrates that it remains in solution and can be detected within the applied voltage range for this solution. The lower collection efficiencies (~60%)

compared to that for FCA/FCA^{+} may be attributed to a weaker reversibility of the Fe^{2+}/Fe^{3+} couple.

Based on the obtained calibration curves and multiple replicates in the background solution, the LOD was calculated to be on the order of 0.01 µM (0.6 µg.L^{-1}). Analysis performed over the same 0 to 40 µM Fe^{2+} range in non-GC mode indicated a significantly higher LOD of 0.44 µM (24.6 µg.L^{-1}) which further demonstrates the benefits of GC mode analysis for Fe^{2+} detection in water. In order to overcome any matrix effects arising from the unknown tap water composition, the iron content was measured using a standard addition technique. In this approach, measurements were carried out for a range of tap water aliquots diluted 1:10 in deionised water spiked with 0.1 to 0.5 µM iron and acidified to pH 3 with HCl. As can be seen in Figure 8 (a), recorded signals display the same shape as that in Figure 7 (a), in particular the gold reduction peak was approximately of the same magnitude as previously seen for all solutions. However the position of the peaks shifted by about 0.1 V (likely due to the slight variability of the platinum quasi-reference electrode), consequently the potential window was adjusted accordingly. As depicted in Figure 8 (b), the peak currents at WE1 were also found to be directly proportional to the iron concentration (R^2 = 0.995) yielding an average iron content of 2.4 ± 1.0 µM.

Figure 8: (a) Typical CVs (vs. Pt) between 0 and 1 V at 100 mV.s^{-1} in aliquots of tap water 1:10 diluted, spiked with 0.1 to 0.5 µM Fe^{2+} and acidified to pH 3 with 1 mM HCl for gold nanowire interdigitated electrode arrays with 500 nm inter-nanowire spacing. Arrays were used in GC mode: the potential of WE1 was swept while the potential of WE2 was held at 0.4 V (vs. Pt). The current was measured at both WE1 (solid lines) and WE2 (dashed lines). (b) Peak currents measured at WE1 vs. Fe^{2+} concentration.

4. Conclusions

Interdigitated gold nanowire electrode arrays with reproducible dimensions (~100 nm wide, ~50 nm high, ~45 μm long and ~500 nm spacing) were fabricated on a Si/SiO_2 chip substrates. When employed in GC mode, interdigitated arrays displayed significantly enhanced electrochemical behaviour arising from RC processes, e.g., fast establishment (within a hundred milliseconds at 5000 $mV.s^{-1}$) of steady-state conditions, increased signal to noise ratios and increased sensitivity while also allowing quantitative detection at much lower concentrations. Simulations of analyte diffusion of the system were in excellent agreement with experimental results. Both simulations and experiments showed that for a relatively simple interdigitated nanowire array exposed to bulk solution the environment of the electrodes could be altered such that the product of the electrochemical reaction can be detected with an amplified signal in GC mode analysis. The neighbouring nanoelectrode can therefore act as a switch for electrochemical responses depending on its imposed potential which opens up a wider range of detection capability for the already versatile electrochemical approach. Finally, the suitability of gold INEAs towards iron sensing was demonstrated in the 0.5 to 40 μM (28 to 2234 $\mu g.L^{-1}$) concentration range with an LOD on the order of 0.01 μM (0.6 $\mu g.L^{-1}$), which is well below the 200 $\mu g.L^{-1}$ permitted_concentration limit for iron in drinking water in Europe.

ACCEPTED MANUSCRIPT

References

[1] A. Biswas, I.S. Bayer, A.S. Biris, T. Wang, E. Dervishi, F. Faupel, Advances in top–down and bottom–up surface nanofabrication: Techniques, applications & future prospects, Adv. Colloid Interface Sci., 170 (2012) 2-27.
[2] K. Dawson, A. O'Riordan, Electroanalysis at the Nanoscale, in: R.G. Cooks, J.E. Pemberton (Eds.) Annual Review of Analytical Chemistry, Vol 72014, pp. 163-+.
[3] C.K. Chua, M. Pumera, Detection of silver nanoparticles on a lab-on-chip platform, Electrophoresis, 34 (2013) 2007-2010.
[4] V. Gubala, L.F. Harris, A.J. Ricco, M.X. Tan, D.E. Williams, Point of Care Diagnostics: Status and Future, Anal. Chem., 84 (2012) 487-515.
[5] S. Barry, K. Dawson, E. Correa, R. Goodacre, A. O'Riordan, Highly sensitive detection of nitroaromatic explosives at discrete nanowire arrays, Faraday Discussions, 164 (2013) 283-293.
[6] K. Dawson, A. Wahl, R. Murphy, A. O'Riordan, Electroanalysis at Single Gold Nanowire Electrodes, The Journal of Physical Chemistry C, 116 (2012) 14665-14673.
[7] S.E.F. Kleijn, A.I. Yanson, M.T.M. Koper, Electrochemical characterization of nano-sized gold electrodes fabricated by nano-lithography, Journal of Electroanalytical Chemistry, 666 (2012) 19-24.
[8] S. Rauf, M.J.A. Shiddiky, A. Asthana, K. Dimitrov, Fabrication and characterization of gold nanohole electrode arrays, Sensors and Actuators B: Chemical, 173 (2012) 491-496.
[9] C. Duarte-Guevara, V.V. Swaminathan, M. Burgess, B. Reddy, E. Salm, Y.-S. Liu, J. Rodriguez-Lopez, R. Bashir, On-chip metal/polypyrrole quasi-reference electrodes for robust ISFET operation, Analyst, 140 (2015) 3630-3641.
[10] K. Dawson, A. Wahl, S. Barry, C. Barrett, N. Sassiat, A.J. Quinn, A. O'Riordan, Fully integrated on-chip nano-electrochemical devices for electroanalytical applications, Electrochimica Acta, 115 (2014) 239-246.
[11] A. Molina, J. Gonzalez, M.C. Henstridge, R.G. Compton, Voltammetry of Electrochemically Reversible Systems at Electrodes of Any Geometry: A General, Explicit Analytical Characterization, The Journal of Physical Chemistry C, 115 (2011) 4054-4062.
[12] D.W.M. Arrigan, Nanoelectrodes, nanoelectrode arrays and their applications, Analyst, 129 (2004) 1157-1165.
[13] A. Wahl, S. Barry, K. Dawson, J. MacHale, A.J. Quinn, A. O'Riordan, Electroanalysis at Ultramicro and Nanoscale Electrodes: A Comparative Study, Journal of The Electrochemical Society, 161 (2014) B3055-B3060.
[14] N. Godino, X. Borrisé, F.X. Muñoz, F.J. del Campo, R.G. Compton, Mass Transport to Nanoelectrode Arrays and Limitations of the Diffusion Domain Approach: Theory and Experiment, The Journal of Physical Chemistry C, 113 (2009) 11119-11125.
[15] A. Wahl, K. Dawson, J. MacHale, S. Barry, A.J. Quinn, A. O'Riordan, Gold nanowire electrodes in array: simulation study and experiments, Faraday Discussions, 164 (2013) 377-390.
[16] C. Schopf, A. Wahl, A. Martin, A. O'Riordan, D. Iacopino, Direct Observation of Mercury Amalgamation on Individual Gold Nanorods Using Spectroelectrochemistry, J. Phys. Chem. C, 120 (2016) 19295-19301.
[17] K. Dawson, A. Wahl, A. Pescaglini, D. Iacopino, A. O'Riordan, Gold Nanowire Electrode Arrays: Investigations of Non-Faradaic Behavior, Journal of the Electrochemical Society, 161 (2014) B3049-B3054.
[18] C.G. Zoski, Handbook of Electrochemistry, Elsevier Science Bv, Amsterdam, 2007.

[19] A.J. Bard, J.A. Crayston, G.P. Kittlesen, T. Varco Shea, M.S. Wrighton, Digital simulation of the measured electrochemical response of reversible redox couples at microelectrode arrays: consequences arising from closely spaced ultramicroelectrodes, Anal. Chem., 58 (1986) 2321-2331.
[20] K. Aoki, M. Morita, O. Niwa, H. Tabei, Quantitative analysis of reversible diffusion-controlled currents of redox soluble species at interdigitated array electrodes under steady-state conditions, Journal of Electroanalytical Chemistry and Interfacial Electrochemistry, 256 (1988) 269-282.
[21] O. Niwa, M. Morita, H. Tabei, Electrochemical behavior of reversible redox species at interdigitated array electrodes with different geometries: consideration of redox cycling and collection efficiency, Anal. Chem., 62 (1990) 447-452.
[22] M. Paeschke, U. Wollenberger, C. Köhler, T. Lisec, U. Schnakenberg, R. Hintsche, Properties of interdigital electrode arrays with different geometries, Analytica Chimica Acta, 305 (1995) 126-136.
[23] M. Paeschke, U. Wollenberger, T. Lisec, U. Schnakenberg, R. Hintsche, Highly sensitive electrochemical microsensensors using submicrometer electrode arrays, Sensors and Actuators B: Chemical, 27 (1995) 394-397.
[24] D. Han, L.P. Zaino, K.Y. Fu, P.W. Bohn, Redox Cycling in Nanopore-Confined Recessed Dual-Ring Electrode Arrays, J. Phys. Chem. C, 120 (2016) 20634-20641.
[25] E. Kätelhön, B. Hofmann, S.G. Lemay, M.A.G. Zevenbergen, A. Offenhäusser, B. Wolfrum, Nanocavity Redox Cycling Sensors for the Detection of Dopamine Fluctuations in Microfluidic Gradients, Anal. Chem., 82 (2010) 8502-8509.
[26] S. Han, J. Zhai, L. Shi, X. Liu, W. Niu, H. Li, G. Xu, Rotating minidisk–disk electrodes, Electrochemistry Communications, 9 (2007) 1434-1438.
[27] M.G. Straver, M. Odijk, W. Olthuis, A. van den Berg, A simple method to fabricate electrochemical sensor systems with predictable high-redox cycling amplification, Lab on a Chip, 12 (2012) 1548-1553.
[28] B. Wolfrum, E. Katelhon, A. Yakushenko, K.J. Krause, N. Adly, M. Huske, P. Rinklin, Nanoscale Electrochemical Sensor Arrays: Redox Cycling Amplification in Dual-Electrode Systems, Accounts Chem. Res., 49 (2016) 2031-2040.
[29] C. Ma, N.M. Contento, L.R. Gibson, P.W. Bohn, Redox Cycling in Nanoscale-Recessed Ring-Disk Electrode Arrays for Enhanced Electrochemical Sensitivity, ACS Nano, 7 (2013) 5483-5490.
[30] D. Han, Y.-R. Kim, C.M. Kang, T.D. Chung, Electrochemical Signal Amplification for Immunosensor Based on 3D Interdigitated Array Electrodes, Anal. Chem., 86 (2014) 5991-5998.
[31] W.H. Organization, Guidelines for drinking-water quality, 2004.
[32] X. Pu, B. Hu, Z. Jiang, C. Huang, Speciation of dissolved iron(ii) and iron(iii) in environmental water samples by gallic acid-modified nanometer-sized alumina micro-column separation and ICP-MS determination, Analyst, 130 (2005) 1175-1181.
[33] A.J. Bard, L.R. Faulkner, Electrochemical Methods : Fundamentals and Applications 2nd edition, (2000).
[34] Y.H. Lanyon, G. De Marzi, Y.E. Watson, A.J. Quinn, J.P. Gleeson, G. Redmond, D.W.M. Arrigan, Fabrication of Nanopore Array Electrodes by Focused Ion Beam Milling, Anal. Chem., 79 (2007) 3048-3055.
[35] R.G. Compton, G.G. Wildgoose, N.V. Rees, I. Streeter, R. Baron, Design, fabrication, characterisation and application of nanoelectrode arrays, Chem. Phys. Lett., 459 (2008) 1-17.
[36] N.V. Rees, R.G. Compton, Voltammetry as a probe of displacement, Chemical Communications, 46 (2010) 4238-4248.

[37] J.H. Thomas, S.K. Kim, P.J. Hesketh, H.B. Halsall, W.R. Heineman, Microbead-based electrochemical immunoassay with interdigitated array electrodes, Analytical Biochemistry, 328 (2004) 113-122.
[38] J.M. Gorell, C.C. Johnson, B.A. Rybicki, E.L. Peterson, G.X. Kortsha, G.G. Brown, R.J. Richardson, Occupational exposure to manganese, copper, lead, iron, mercury and zinc and the risk of Parkinson's disease, Neurotoxicology, 20 (1999) 239-247.
[39] A. Bradman, B. Eskenazi, P. Sutton, M. Athanasoulis, L.R. Goldman, Iron deficiency associated with higher blood lead in children living in contaminated environments, Environmental Health Perspectives, 109 (2001) 1079-1084.
[40] E.S. Gurzau, C. Neagu, A.E. Gurzau, Essential metals—case study on iron, Ecotoxicology and Environmental Safety, 56 (2003) 190-200.
[41] E.A. Zakharova, E.E. Elesova, G.N. Noskova, M. Lu, R.G. Compton, Direct Voltammetric Determination of Total Iron with a Gold Microelectrode Ensemble, Electroanalysis, 24 (2012) 2061-2069.
[42] L.D. Burke, Scope for new applications for gold arising from the electrocatalytic behaviour of its metastable surface states, Gold Bull, 37 (2004) 125-135.

ACCEPTED MANUSCRIPT

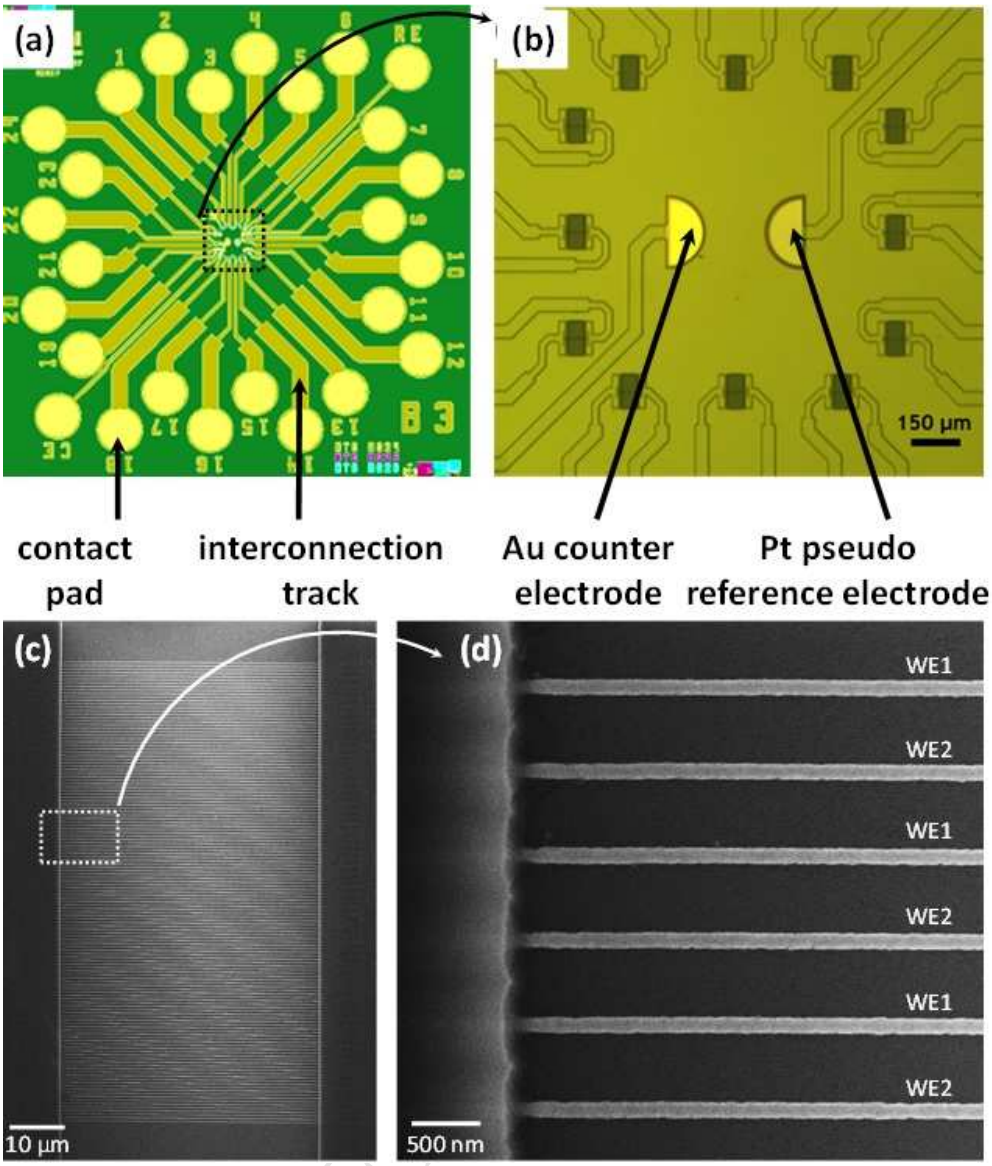

ACCEPTED MANUSCRIPT

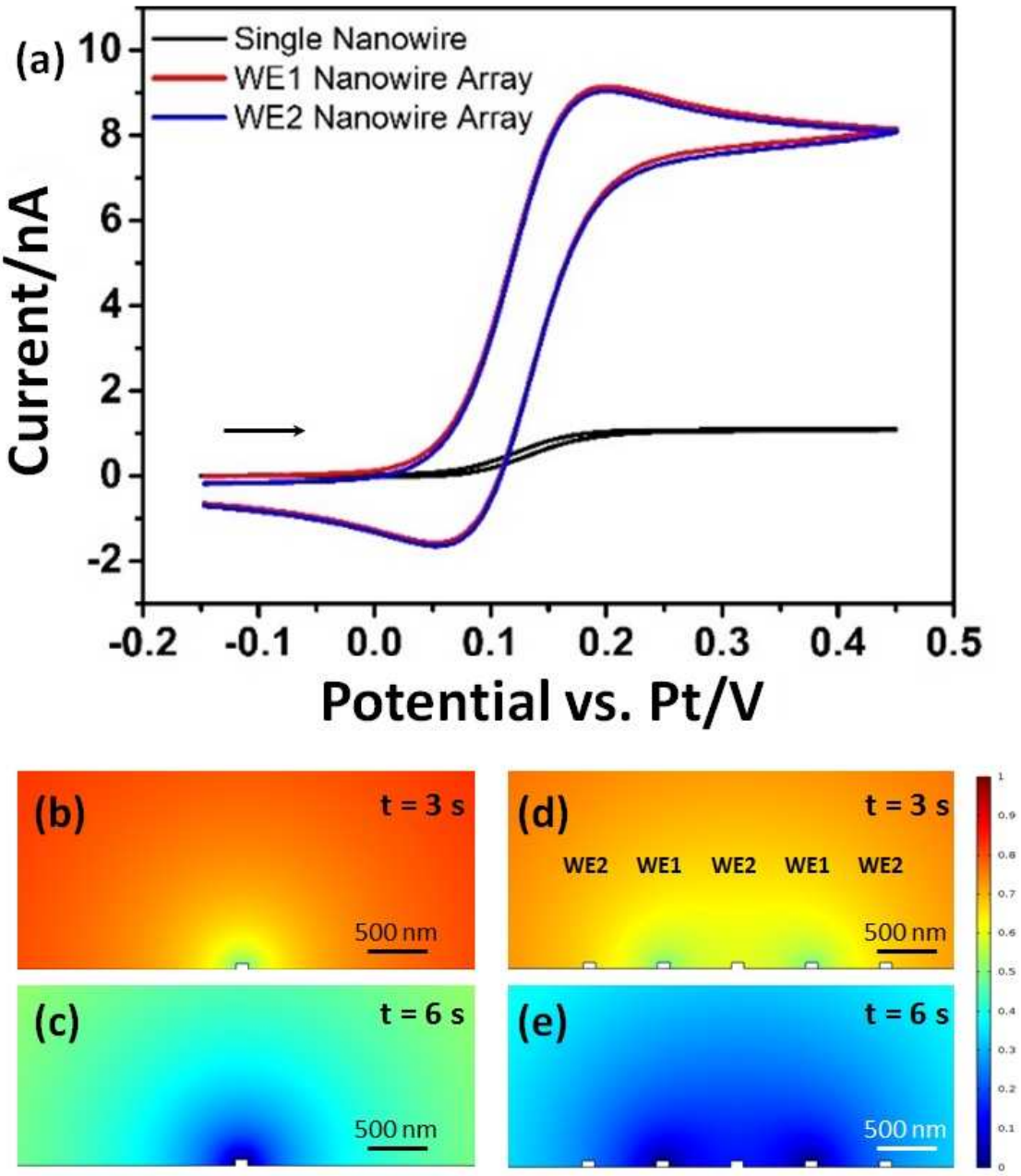
(a)
Single Nanowire
WE1 Nanowire Array
WE2 Nanowire Array
Current/nA
Potential vs. Pt/V
10
8
6
4
2
0
-2
-0.2
-0.1
0.0
0.1
0.2
0.3
0.4
0.5
(b)
t = 3 s
500 nm
(d)
t = 3 s
WE2
WE1
WE2
WE1
WE2
500 nm
(c)
t = 6 s
500 nm
(e)
t = 6 s
500 nm

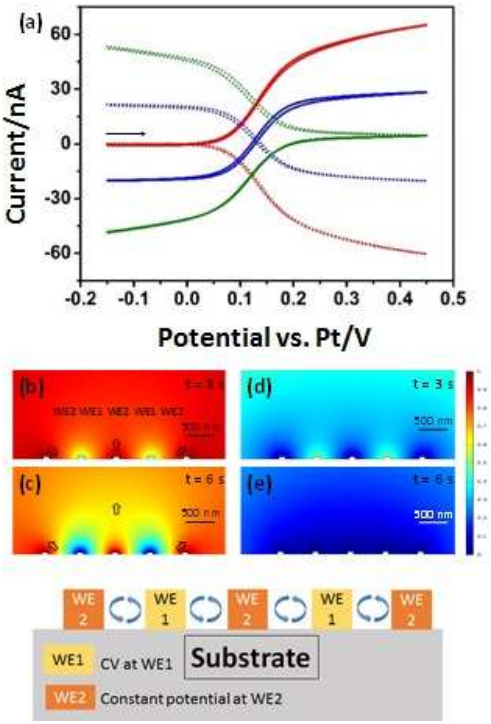

ACCEPTED MANUSCRIPT

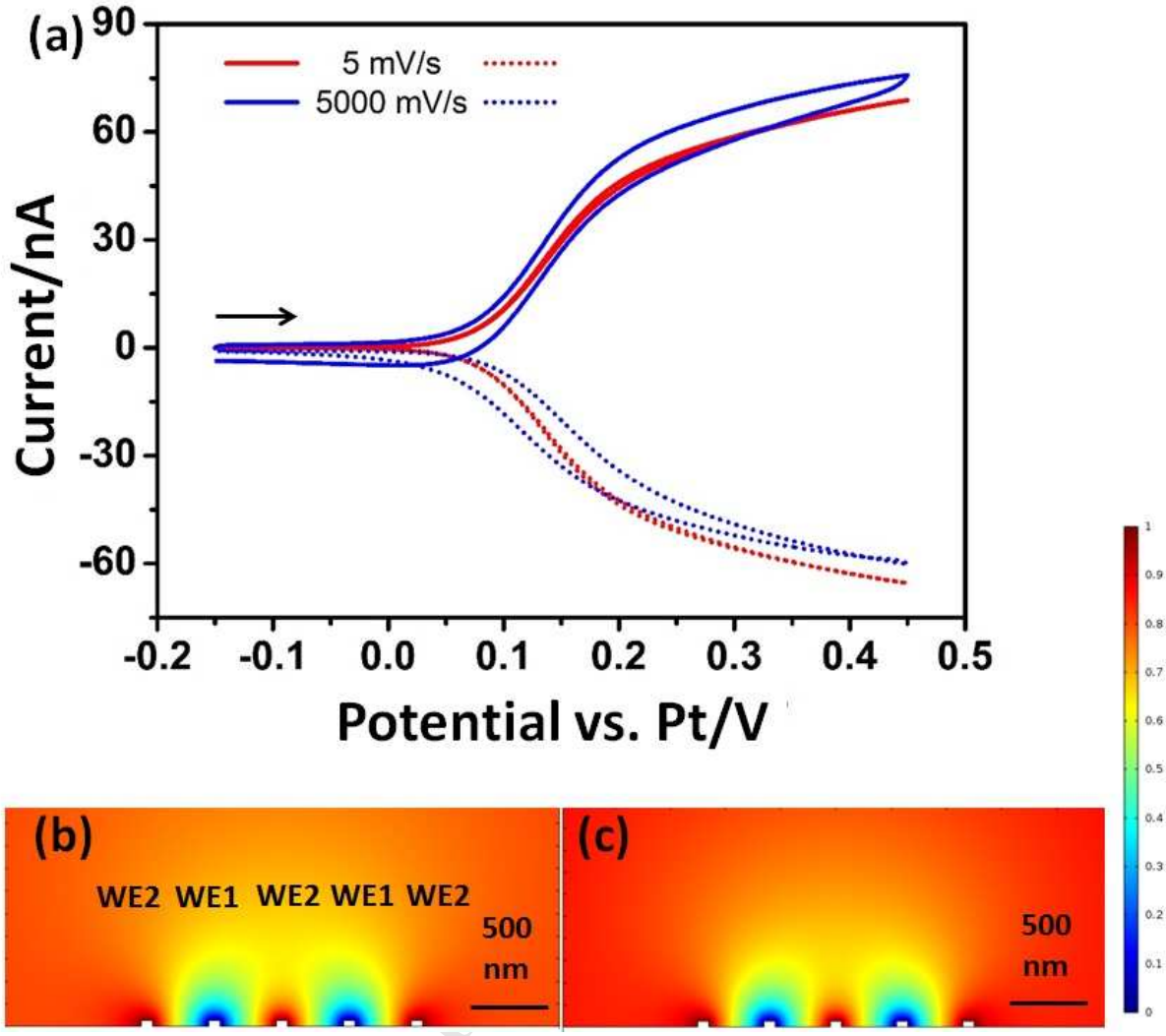

ACCEPTED MANUSCRIPT

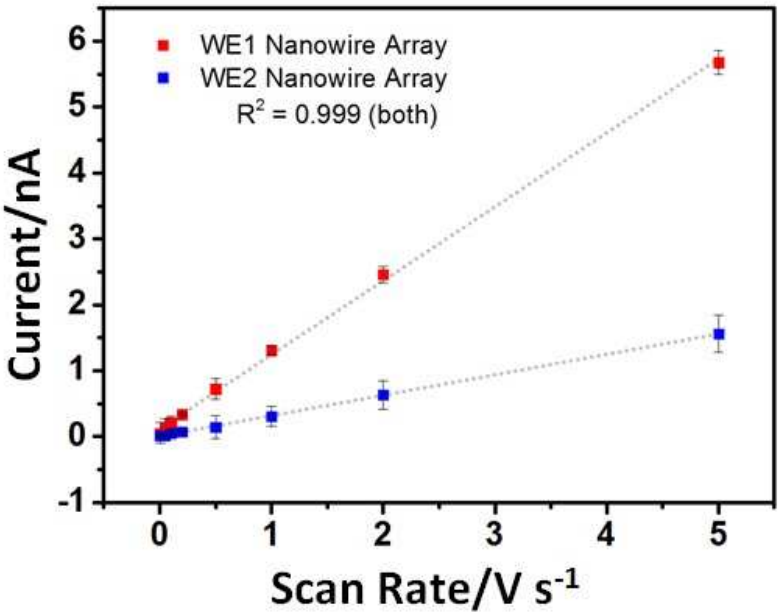

ACCEPTED MANUSCRIPT

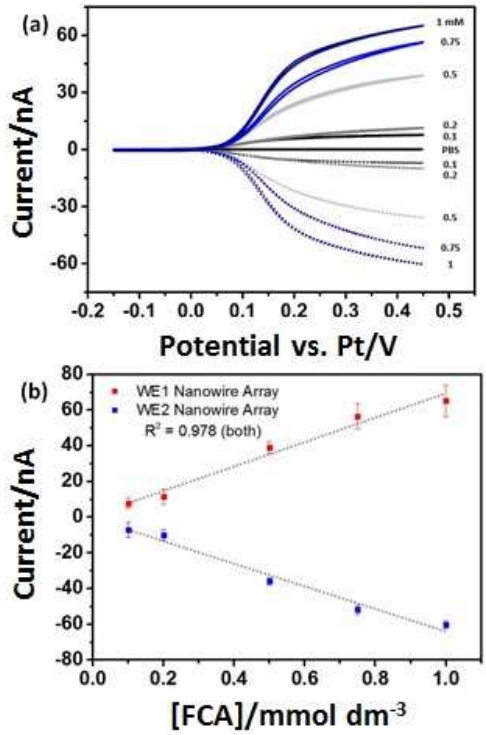

ACCEPTED MANUSCRIPT

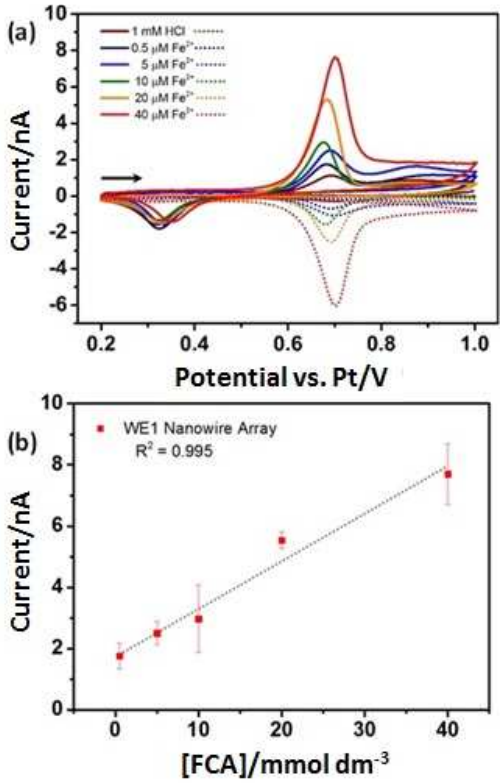

ACCEPTED MANUSCRIPT

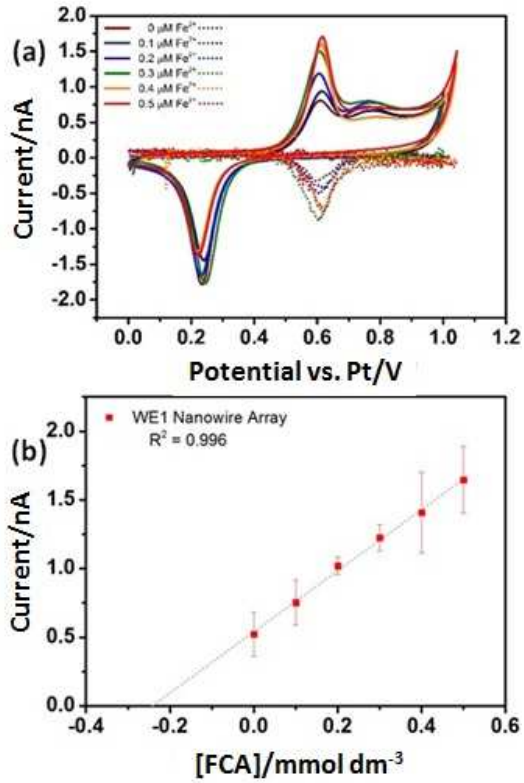

ACCEPTED MANUSCRIPT

- When employed in generator-collector mode, interdigitated nanoelectrode arrays displayed significantly enhanced electrochemical behaviour arising from redox cycling processes, e.g., fast establishment (within a hundred milliseconds at 5000 $mV.s^{-1}$) of steady-state conditions.
- Simulations of analyte diffusion were in excellent agreement with experimental results.
- Both simulations and experiments showed that for a relatively simple interdigitated nanowire array exposed to bulk solution the environment of the electrodes could be altered such that the product of the electrochemical reaction can be detected with an amplified signal in GC mode analysis.
- The suitability of the nanoelectrode array to iron sensing was demonstrated in the 0.5 to 40 µM (28 to 2234 $\mu g.L^{-1}$) concentration range with an LOD on the order of 0.01 µM (0.6 $\mu g.L^{-1}$), which is well below the 200 $\mu g.L^{-1}$ permitted concentration limit for iron in drinking water in Europe.

ACCEPTED MANUSCRIPT